Results in Engineering 26 (2025) 104824

Contents lists available at ScienceDirect

Results in Engineering

journal homepage: www.sciencedirect.com/journal/results-in-engineering

Research paper

Synthesis, Characterization, and Enhanced Optical and Dielectric Properties of Pure and Ni-Doped ZnO Nanoparticles for Advanced Electronic Applications

Muhammad Fawad [a], Nabeel Maqsood [b,c,*], Ahmad Nawaz [d], Bilal Islam [c], Malik Daniyal Zaheer [e], Kateřina Skotnicová [b]

[a] Department of Physics, University of Peshawar, Postcode 25120, Peshawar, KPK, Pakistan
[b] Faculty of Materials Science and Technology, VSB – Technical University of Ostrava, 17. listopadu 2172/15, 708 00 Ostrava, Czech Republic
[c] Department of Laser Technologies, Center for Physical Sciences and Technology, Savanoriu Ave. 231, LT-02300, Vilnius, Lithuania
[d] Department of Mechanical Engineering, University of Engineering & Technology, Peshawar, Pakistan
[e] Faculty of Mechanical Engineering and Design, Kaunas University of Technology, Kaunas, LT-51424, Lithuania

ARTICLE INFO

Keywords:
Nickel-Doped Zinc Oxide (Ni:ZnO)
Nanoparticle Characterization
Co-Precipitation Method
Optical and Dielectric Properties
Burstein-Moss Effect

ABSTRACT

Nickel (Ni)-doped zinc oxide (ZnO) nanoparticles have garnered significant attention due to their tunable structural, optical, and electronic properties, making them ideal candidates for various advanced applications. This study focuses on the synthesis, characterization, and evaluation of the electrical and electronic properties of pure and Ni-doped ZnO nanoparticles (Ni:ZnO) synthesized via a co-precipitation method with varying Ni concentrations (2%, 4%, 6%, and 8%). X-ray diffraction analysis confirmed the wurtzite hexagonal structure of ZnO, with lattice distortion increasing proportionally to Ni doping. A secondary NiO phase was detected at higher doping levels, indicating the solubility limit of Ni in ZnO. The average crystallite size, calculated using Debye-Scherrer's equation, decreased from 31 nm in pure ZnO to 23 nm in 8% Ni-doped ZnO, confirming doping-induced size reduction. UV-visible spectroscopy revealed a blue shift in the optical bandgap from 3.23 eV for pure ZnO to 3.41 eV for 8% Ni-doped ZnO, attributed to Burstein-Moss effect. Fourier transform infrared spectroscopy identified changes in vibrational modes, with shifts in peaks corresponding to Zn-O and Ni-O bonds, indicating successful Ni incorporation. Scanning electron microscopy (SEM) and energy-dispersive X-ray spectroscopy confirmed uniform particle morphology and elemental composition. Dielectric studies showed that the dielectric constant increased significantly with Ni doping, reaching a maximum value of 69 at 6% doping, while AC conductivity improved with frequency, demonstrating frequency-dependent conductivity due to hopping charge carriers. The findings reveal that Ni doping enhances the structural, optical, and dielectric properties of ZnO, making it suitable for optoelectronics, high-frequency devices, and dielectric materials.

1. Introduction

Zinc oxide (ZnO), a II-VI semiconductor with a direct wide bandgap of 3.37 eV at room temperature, has been extensively studied for its versatile applications in optoelectronics, photocatalysis, sensors, and energy devices [1–4]. Its high exciton binding energy of 60 meV allows efficient excitonic emissions at room temperature, making ZnO a promising material for ultraviolet (UV) lasers, light-emitting diodes (LEDs), and photodetectors [5,6]. The unique combination of high optical transparency, piezoelectricity, and chemical stability further broadens its industrial relevance [7,8].

Due to its large band gap ZnO has followings advantages, higher breakdown voltage values, supporting of large electric fields, high temperature and power operations. ZnO (3.37eV) and GaN (3.39eV) both have large band gap semiconductors however ZnO has some significant advantages in its large free exciton binding energy 60meV compared to 25meV for GaN that allows for efficient excitonic emission at room temperature [5]. This is one of the significant parameters due to which ZnO shows lasing emission at room temperature.

ZnO nanostructures, including nanoparticles, nanowires, and thin

---

* Corresponding author.
E-mail addresses: mfawad@gmail.com (M. Fawad), nabeel.maqsood@vsb.cz (N. Maqsood), ahmadnawaz@uetpeshawar.edu.pk (A. Nawaz), bilal.islam@ftmc.lt (B. Islam), malik.zaheer@ktu.edu (M.D. Zaheer), katerina.skotnicova@vsb.cz (K. Skotnicová).

https://doi.org/10.1016/j.rineng.2025.104824
Received 7 February 2025; Received in revised form 23 March 2025; Accepted 5 April 2025
Available online 6 April 2025
2590-1230/© 2025 The Authors. Published by Elsevier B.V. This is an open access article under the CC BY-NC license (http://creativecommons.org/licenses/by-nc/4.0/).

films, exhibit remarkable physical and chemical properties due to their large surface-to-volume ratio, quantum confinement effects, and tunable morphology [9,10]. These properties make ZnO highly advantageous for gas sensing, where its surface reactivity facilitates selective detection of gases like NO_2 and CO, as well as for photocatalysis, where its wide bandgap supports efficient charge carrier separation and UV absorption [11,12]. However, the intrinsic properties of ZnO often require modification to optimize its performance for specific applications [13,14].

Due to addition of other elements by very small quantities called dopants to the intrinsic material we can modify electronic and conductivity property by an organized manner. Such process by which we can change electronic and conductivity property by well manner we called it doping. Semiconductor material defining property is that it can be doped with impurities with very small amount. These small, doped impurities changed its physical and chemical properties in a controllable way. Maximum used semiconductor materials are crystalline and inorganic in nature [15].

Doping ZnO with metal or non-metal elements has proven to be an effective strategy to enhance its structural, optical, and electronic properties. Transition metals such as cobalt (Co), manganese (Mn), and nickel (Ni) are particularly effective dopants, as they introduce localized states in the bandgap, thereby modifying electrical conductivity, magnetic behavior, and optical absorption [16–18]. Nickel-doped ZnO (Ni: ZnO) nanoparticles have attracted significant attention due to their potential applications in spintronics, high-performance gas sensors, and high-frequency dielectric materials [19,20]. Nickel doping in ZnO introduces Ni^{2+} ions into the ZnO lattice, substituting Zn^{2+} due to their comparable ionic radii (0.69 Å for Ni^{2+} and 0.74 Å for Zn^{2+}) [21]. This substitution leads to lattice distortion and the introduction of defect states, such as oxygen vacancies, which play a critical role in modulating the electrical and optical properties of ZnO [22]. At low doping concentrations, Ni^{2+} ions are homogeneously distributed within the ZnO lattice, enhancing conductivity and optical transparency through the Burstein-Moss effect, where the Fermi level shifts into the conduction band due to increased carrier concentration [23,24]. However, at higher doping levels, NiO secondary phases can emerge, adversely affecting the structural and electronic uniformity [25,26]. The optical properties of Ni-doped ZnO are also significantly influenced by doping. Studies have reported a blue shift in the optical absorption edge with increasing Ni concentration due to the widening of the optical bandgap (Burstein-Moss effect) [27]. Simultaneously, doping alters photoluminescence characteristics, typically reducing defect-related emissions and enhancing near-band-edge emissions, which is beneficial for optoelectronic applications [28].

Nickel doping is known to impact the dielectric behavior of ZnO. Enhanced dielectric constant and reduced dielectric loss have been observed in Ni-doped ZnO due to the introduction of charge carriers and interfacial polarization at grain boundaries [29,30]. Additionally, doping influences AC conductivity, which exhibits a frequency-dependent behavior linked to the hopping mechanism of charge carriers between localized states. Such properties are critical for applications in high-frequency electronics and capacitors [31,32].

Several studies have explored the synthesis and characterization of Ni-doped ZnO nanoparticles. Ahmed et al. demonstrated that Ni doping enhances photocatalytic activity by increasing defect density and charge carrier mobility [33]. U. Godavarti et al. reported the role of Ni doping in improving ZnO's gas sensing performance by altering its surface reactivity and defect distribution [34]. Despite these advances, most research has been limited to low doping concentrations (1–5%), and the effects of higher Ni doping levels on phase formation, optical properties, and dielectric behavior remain underexplored.

While the literature establishes the significance of Ni doping in tailoring ZnO's properties, gaps persist in understanding its effects at higher doping levels (≥6%). The formation of secondary phases, such as NiO, and their influence on structural, optical, and dielectric properties require further investigation. Additionally, the relationship between Ni doping and AC conductivity, particularly at high frequencies, is not well understood.

This study aims to synthesize and comprehensively characterize pure and Ni-doped ZnO nanoparticles with varying Ni concentrations (2–8%). By focusing on high doping levels, the work seeks to unravel the effects of Ni incorporation on the structural, optical, and dielectric properties of ZnO. The novelty of the study lies in its detailed analysis of secondary phase formation, bandgap tuning, dielectric behavior, and AC conductivity, offering new insights into the potential applications of Ni-doped ZnO in optoelectronic and high-frequency dielectric devices.

2. Methodology

2.1. Synthesis of Pure and Ni-Doped ZnO Nanoparticles

Pure and nickel (Ni)-doped zinc oxide (ZnO) nanoparticles were synthesized using a co-precipitation method. Analytical-grade zinc acetate dihydrate ($Zn(CH_3COO)_2{\cdot}2H_2O$) was used as the precursor for zinc ions, while nickel nitrate hexahydrate ($Ni(NO_3)_2{\cdot}6H_2O$) was used as the source of nickel ions. Sodium hydroxide (NaOH) was employed as the precipitating agent. All chemicals were of high purity and used without further purification.

Firstly, a 0.2 M solution of zinc acetate dihydrate was prepared in deionized water. For Ni-doped ZnO, the required amounts of nickel nitrate hexahydrate (2%, 4%, 6%, and 8% molar ratios relative to zinc ions) were dissolved in the zinc acetate solution with constant stirring. Sodium hydroxide solution (0.5 M) was added dropwise into the precursor solution under continuous stirring until the pH of the solution reached approximately 10, facilitating the precipitation of $Zn(OH)_2$ and $Ni(OH)_2$. The mixture was stirred at room temperature for 2 hours to ensure complete precipitation.

The precipitate was aged for 24 hours, followed by repeated washing with deionized water and ethanol to remove impurities and residual ions. The washed precipitate was dried at 80°C in an air oven for 12 hours. The dried powder was calcined at 500°C for 3 hours in a muffle furnace to obtain crystalline pure and Ni-doped ZnO nanoparticles. The synthesis method is explained in flow chart form in Fig. 1.

2.2. Characterization Techniques

After the synthesis of undoped and nickel doped ZnO nanoparticles different characterization techniques were used to check their structural, optical and dielectric properties.

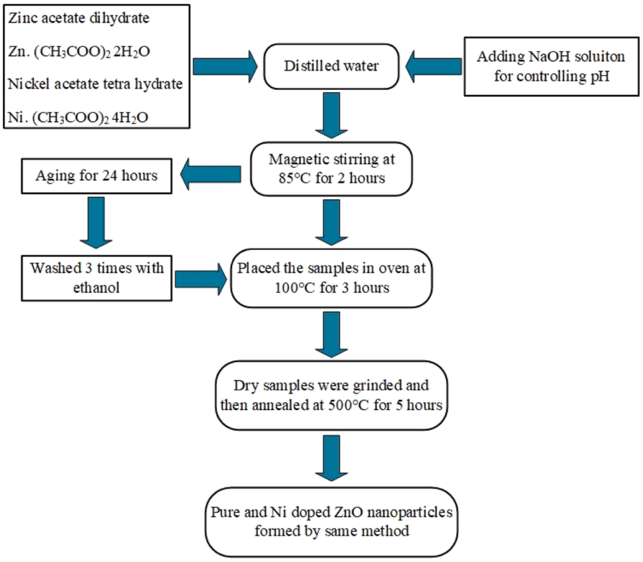

Fig. 1. Experimental setup for the synthesis process.

2.2.1. *Fourier Transform Infrared (FTIR) Spectroscopy*

FTIR analysis was conducted in the range of 400–4000 cm^{-1} to identify functional groups and confirm Ni doping by detecting vibrational changes in Zn-O and Ni-O bonds.

2.2.2. *X-ray Diffraction (XRD) Analysis*

The structural properties of the synthesized nanoparticles were studied using XRD with Cu-Kα radiation (λ = 1.5406 Å) in the 2θ range of 20°–80°. The crystallite size (D) was calculated using Debye-Scherrer's equation:

$$D = \frac{K\lambda}{\beta\ cos\theta} \tag{1}$$

where K is the shape factor (0.9), λ is the X-ray wavelength, β is the full width at half maximum (FWHM) of the diffraction peak, and θ is the Bragg angle. Lattice parameters and phase purity were also analyzed.

2.2.3. *Scanning Electron Microscopy (SEM) and Energy-Dispersive X-ray Spectroscopy (EDX)*

SEM was used to analyze the surface morphology and particle size of the nanoparticles. EDX was employed to determine the elemental composition and confirm the incorporation of Ni into the ZnO lattice.

2.3. *Diffused reflective spectroscopy (DRS) analysis*

Calculating the band gap from diffuse reflection data, the Kubelka-Munk equation was used to find the absorption coefficient from reflection. The absorption coefficient can be defined as the measure of photons absorption per thickness of a material. The unit of absorption coefficient is (cm^{-1}). The Kubelka-Munk equation is given as

$$\frac{\alpha}{S} = \frac{(1-R)^2}{2R} \tag{2}$$

Thus

$$\alpha = \frac{S(1-R)^2}{2R} \tag{3}$$

Here "S" is a scattering coefficient which measures the ability of a particle to scatter a beam of photons and it is (cm^{-1}) because scattering coefficient is equal to cross sectional area divided by volume. The energy of a photon can be calculated by a given equation

$$\mathrm{E} = \mathrm{h}\nu = \mathrm{hc}\Big/\lambda = \frac{1240}{\lambda}(\mathrm{eV}) \tag{4}$$

In semiconductors, the optical bandgap is determined using the Tauc plot method, which is widely employed to evaluate electronic transitions. A Tauc plot involves graphing the square of the product of the absorption coefficient (α) and photon energy (E) i.e., $(\alpha E)^2$ against photon energy (E). The curve generated from this data typically contains a segment of a straight line. By extending this straight-line segment to intersect the x-axis, the x-intercept provides the optical bandgap (Eg) of the material. This method is particularly effective for analyzing direct bandgap semiconductors.

2.4. *Dielectric Property Measurements*

The dielectric properties of the samples were analyzed using an impedance analyzer over a frequency range of 10 Hz to 1 MHz. Measurements were conducted at room temperature to evaluate the dielectric constant ($\in_r$), dielectric loss ($tan\ \delta$), and AC conductivity (σ_{AC}). The dielectric constant was calculated using the formula:

$$\in_r = \frac{C.d}{\in_0 A} \tag{5}$$

where C is the capacitance, d is the thickness of the sample, A is the area of the electrode, and $\in_0$ is the permittivity of free space.

The synthesized powders were pressed into pellets of 10 mm diameter and ~2 mm thickness using a hydraulic press under a pressure of 5 tons. The pellets were sintered at 500°C for 2 hours to enhance mechanical stability and electrical connectivity. For dielectric measurements, both sides of the pellets were coated with silver paste to form electrodes, ensuring good electrical contact.

2.5. *AC Conductivity*

AC conductivity (σ_{AC}) was determined using the relation:

$$\sigma_{AC} = 2\pi f \in_0 \in_r tan\ \delta \tag{6}$$

where f is the frequency, $\in_r$ is the dielectric constant, and $tan\ \delta$ is the dielectric loss.

3. Results and Discussions

3.1. *FTIR analysis*

The FTIR analysis was conducted to identify the functional groups and molecular interactions in undoped and Ni-doped ZnO nanoparticles. The full transmittance spectra, ranging from 400 to 4000 cm^{-1}, are presented in Fig. 2. The observed absorption peaks provide detailed insights into the chemical composition and structural modifications induced by nickel doping.

Low-intensity absorption peaks observed around 3480, 2350, and 2950 cm^{-1} are attributed to O-H stretching vibrations, CO_2 molecules, and C-H stretching modes, respectively [35]. These peaks suggest the presence of hydroxyl groups, atmospheric CO_2, and minor organic residues from precursors or synthesis processes. A distinct absorption peak at 1400 cm^{-1} is related to acetate species (COO^-), confirming the presence of residual acetate groups from the zinc acetate precursor [36]. Additionally, a sharp band around 1500 cm^{-1} corresponds to H-O-H bending vibrations, which may arise from trace amounts of adsorbed moisture on the ZnO nanoparticle surface [37].

Vibrational modes associated with ZnO were observed between 698 cm^{-1} and 721 cm^{-1}, corresponding to the Zn-O stretching vibrations [38]. In Ni-doped ZnO samples, a blue shift in the absorption bands was observed as the nickel doping concentration increased. This shift reflects the disturbance of the Zn-O network due to Ni incorporation, indicating an increase in bond strength with higher Ni concentrations. The deviation in vibrational frequencies can be attributed to two factors: (i) the difference in ionic radii between Zn^{2+} (0.74 Å) and Ni^{2+} (0.69 Å), causing lattice distortion, and (ii) structural changes induced by the substitution of Zn with Ni ions [39].

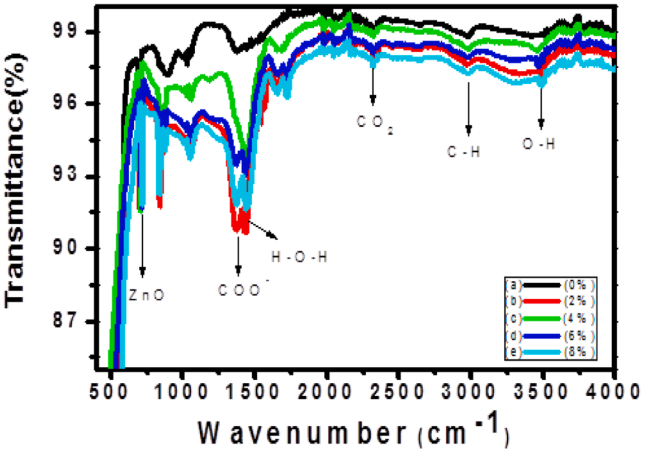

Fig. 2. FTIR transmission spectra for undoped and Ni doped ZnO nanoparticles.

3.2. XRD analysis

The X-ray diffraction (XRD) patterns of undoped, 2%, and 4% Ni-doped ZnO nanoparticles confirmed the presence of a hexagonal wurtzite structure, as indicated by the diffraction peaks that perfectly match the standard JCPDS card No. 36-1451. The lattice parameters were determined to be a =3.249 Å, c = 5.206 Å, with a space group of $P6_3mc$. Up to a doping concentration of 4% (x = 0.04), no additional peaks corresponding to nickel metal, nickel oxide (NiO), or any binary Zn-Ni phases were observed, suggesting complete incorporation of Ni into the ZnO lattice without phase segregation.

However, when the Ni doping concentration increased to 6% (x ≥ 0.06), a new diffraction peak emerged at 2θ ~ 42°, as shown in Fig. 3. This peak corresponds to the (200) Miller indices of NiO, matching the standard JCPDS card No. 78-0643. The intensity of this secondary phase peak increased with higher Ni concentrations, indicating the progressive formation of NiO as the doping level rose. The emergence of this secondary phase demonstrates the solubility limit of Ni in the ZnO lattice, which is less than 6% for the $Zn_{1-x}Ni_xO$ nanoparticles. Beyond this limit, phase segregation occurs, confirming the limited miscibility of Ni in ZnO. In contrast, at lower concentrations (0%, 2%, 4%) Ni would not considerably alter the Zn sites or in other words, Ni incorporates in ZnO lattice without forming any secondary phase. However, at higher concentrations can lead to formation of new phase/s which is also evident from literature [40–42].

The crystallite size of undoped and nickel doped ZnO nanoparticles were calculated by using Debye-Scherer's equation [43]. The results indicate a reduction in crystallite size with increasing Ni doping, attributed to lattice strain induced by the substitution of smaller Ni^{2+} ions (0.69 Å) in place of Zn^{2+} ions (0.74 Å) in the ZnO lattice.

From Fig. 4, it is evident that the crystallite size decreases with increasing Ni concentration, which can be attributed to the surface reaction competition during the synthesis process [44]. This reduction in crystallite size is primarily a result of the stronger bond energy of Ni-O compared to Zn-O. The bond dissociation energy for Ni-O (391 kJ/mol) exceeds that of Zn-O (284 kJ/mol), indicating that Ni^{2+} ions form more stable bonds with oxygen. As a result, the substitution of Zn^{2+} ions with smaller Ni^{2+} ions (ionic radii: 0.69 Å for Ni^{2+} vs. 0.74 Å for Zn^{2+} induces lattice strain and inhibits crystal growth. This stronger Ni-O bonding creates localized regions of higher stability within the ZnO matrix, which restricts the mobility of atoms during crystal growth, resulting in smaller crystallites. Additionally, the enhanced surface energy caused by the smaller size of Ni-doped ZnO particles promotes the formation of smaller crystallites due to the competition between surface energy minimization and bulk crystal growth.

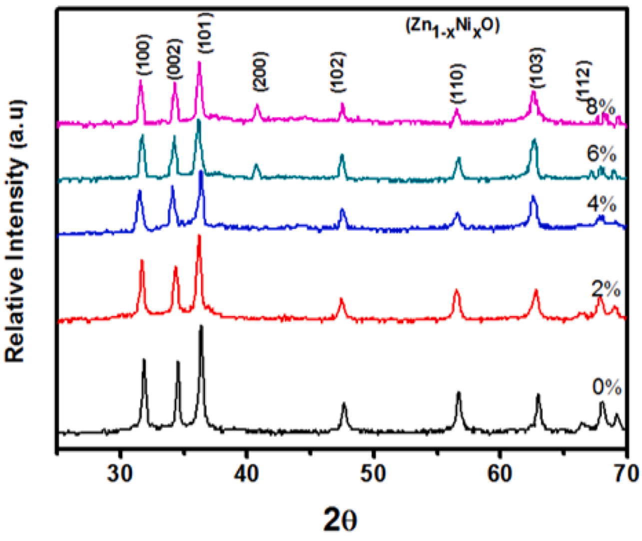

Fig. 3. XRD pattern for (a) 0% (b) 2% (c) 4% (d) 6% and (e) 8% Ni doped ZnO Nanoparticles.

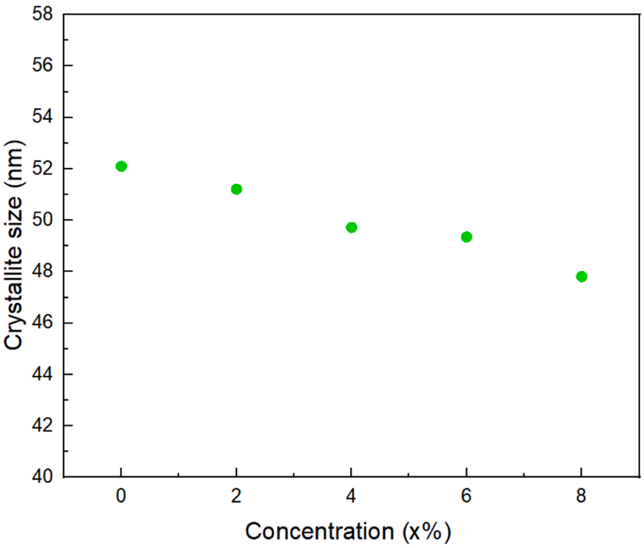

Fig. 4. Crystallite size of pure and Ni doped ZnO nanoparticles.

The observed decrease in crystallite size with Ni doping underscores the critical role of bond energy differences and lattice strain in tuning the structural properties of ZnO nanoparticles. These effects have significant implications for the material's optical, electronic, and catalytic performance, where smaller crystallite size often leads to enhanced surface reactivity and quantum confinement effects.

3.3. SEM and EDX analysis

The surface morphology of $Zn_{1-x}Ni_xO$ nanoparticles with x = 0%, 2%, 4%, 6%, and 8%, is depicted in Fig. 5. The SEM images reveal that both undoped and Ni-doped ZnO nanoparticles are uniformly distributed and exhibit sizes within the nanometer range. The observed morphology indicates that the crystallites predominantly possess a spherical shape, reflecting the isotropic growth behavior of the ZnO nanostructures during synthesis. The SEM analysis confirms that doping with nickel does not significantly alter the overall morphology of the particles, maintaining their spherical structure across all doping concentrations. Furthermore, the nanometer-scale size of the particles observed in the SEM images highlights the efficacy of the co-precipitation method in producing nanoparticles with controlled size and uniform distribution.

The consistent nanometer-scale morphology, even with increasing Ni concentrations, indicates that nickel incorporation occurs uniformly in the ZnO lattice without causing agglomeration or significant deviations in particle shape. This uniformity is essential for applications where high surface area and consistent particle size contribute to enhanced optical, electronic, and catalytic properties.

The purity and elemental composition of undoped and Ni-doped ZnO nanoparticles ($Zn_{1-x}Ni_xO$) were confirmed using EDX. The EDX spectra for samples with x = 0%, 2%, 4%, 6%, and 8% are presented in Fig. 6. The analysis identified Zn, Ni, and O as the primary elements in all samples, confirming the absence of impurities and the successful doping of Ni into the ZnO lattice.

The atomic percentages of Zn, Ni, and O for each sample are summarized in Table 1. The results show that the peak intensity of Ni increases systematically with increasing Ni concentration, indicating successful incorporation of Ni ions into the ZnO matrix. The atomic ratio of Ni to Zn (Ni/Zn) was calculated as 0.0033, 0.0631, 0.0996, and 0.1319 for 2%, 4%, 6%, and 8% Ni-doped samples, respectively. These values closely align with the nominal stoichiometric ratios used during

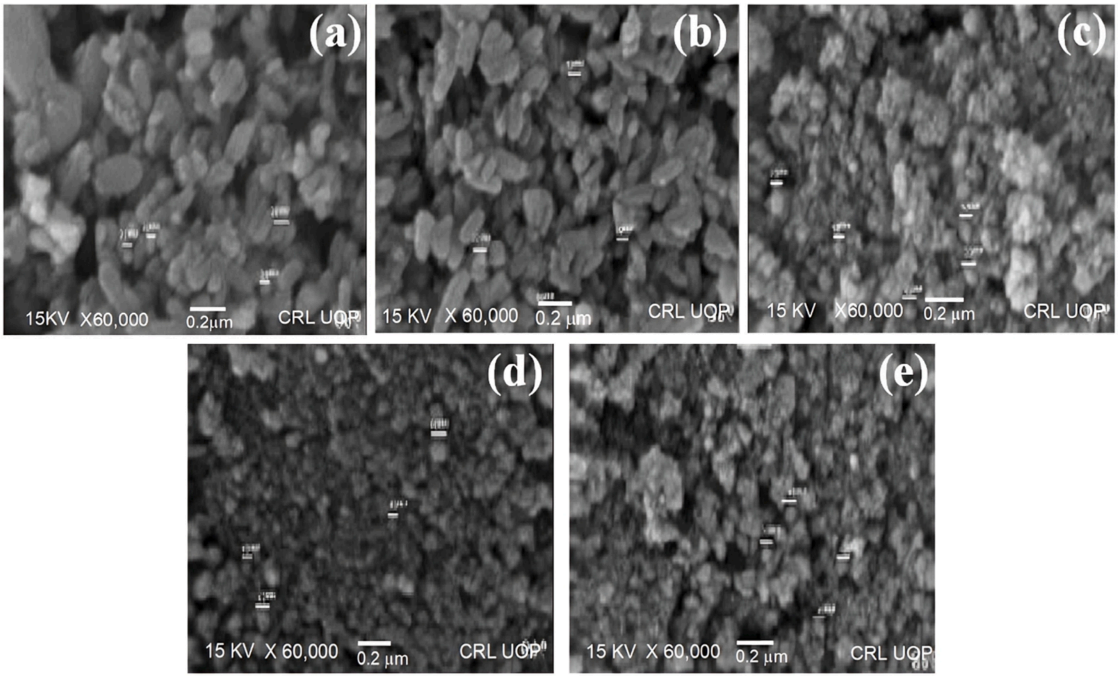

Fig. 5. SEM images of undoped and Ni doped ZnO nanoparticles (a) 0%, (b) 2%, (c) 4%, (d) 6% and (e) 8%.

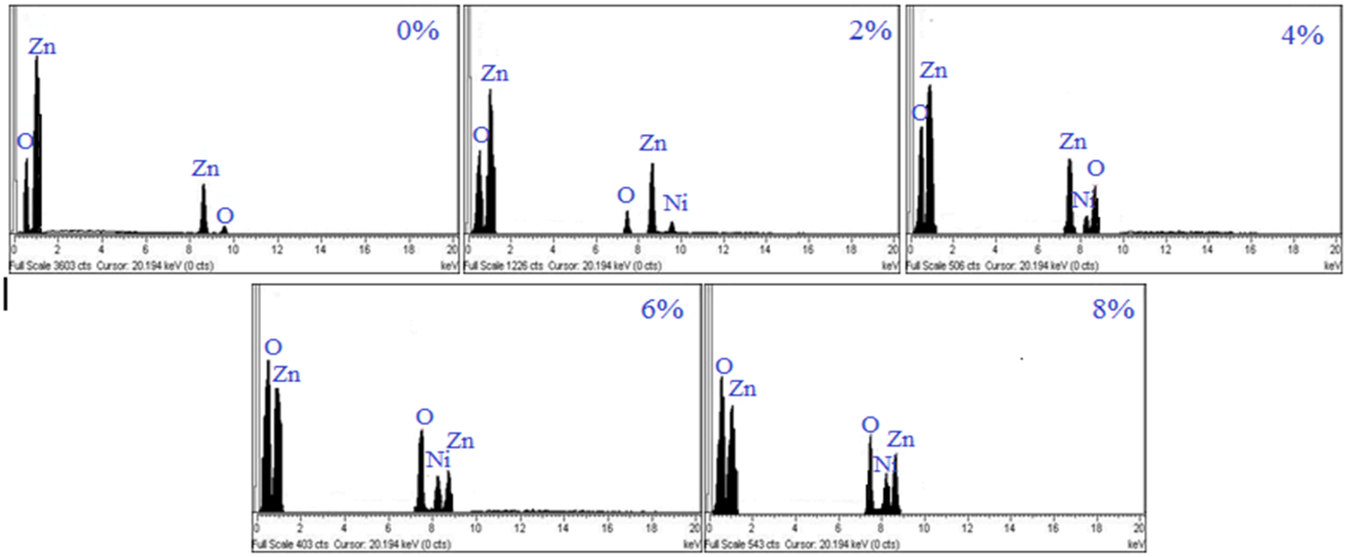

Fig. 6. EDX spectra for (a) undoped (b) 2% (c) 4% (d) 6% and (e) 8% Ni doped ZnO nanoparticles.

Table 1
Compositional elements percentage presents in different concentration samples.

Sample	Percentage of Elements % atomic (%)			
	Zn	O	Ni	Ni/Zn ratio
ZnO	72.69	27.31	-	-
$Zn_{0.99}Ni_{0.02}O$	60.12	39.68	0.20	0.0033
$Zn_{0.97}Ni_{0.04}O$	55.62	40.88	3.51	0.0631
$Zn_{0.95}Ni_{0.06}O$	43.45	52.23	4.32	0.0994
$Zn_{0.93}Ni_{0.08}O$	39.33	55.48	5.19	0.1319

synthesis, demonstrating the accuracy and reliability of the doping process. The EDX analysis confirms that the elemental composition of the $Zn_{1-x}Ni_xO$ nanoparticles is consistent with the intended experimental design. Furthermore, the data support the uniform distribution of nickel within the ZnO system, without evidence of contamination or unintended secondary phases within the detection limits of the technique. This agreement between experimental and theoretical concentrations establishes the suitability of the co-precipitation method for producing high-purity, compositionally accurate Ni-doped ZnO nanoparticles.

3.4. *DRS analysis*

The optical bandgaps of undoped and Ni-doped ZnO nanoparticles were determined using this technique, as shown in Fig. 7. The results indicate that Ni doping affects the optical bandgap, leading to a broadening of the gap, especially in heavily doped samples. This broadening is attributed to the Burstein-Moss effect, which occurs in heavily doped semiconductors. In this phenomenon, the donor electrons

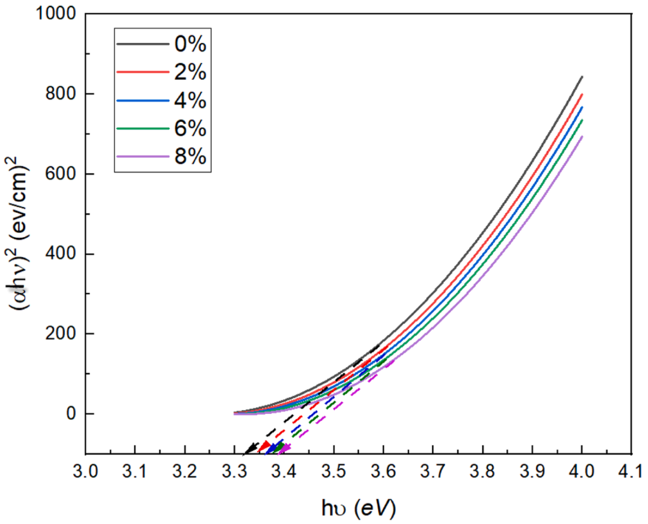

Fig. 7. Optical band gap of undoped and Ni doped ZnO nanoparticles determined by Tauc plot.

occupy all the available energy states at the bottom of the conduction band, effectively blocking low-energy transitions from the valence band to the conduction band. This shift results in an increase in the apparent bandgap energy.

The Burstein-Moss effect is a direct consequence of the Pauli Exclusion Principle, which dictates that no two electrons can occupy the same quantum state simultaneously. As a result, the energy separation between the top of the valence band and the unoccupied states in the conduction band increases, leading to a shift in the optical bandgap [45].

This energy shift occurs due to the positioning of donor and acceptor energy levels relative to the conduction and valence bands in semiconductors. For heavily n-type doped materials, the donor energy levels lie close to the conduction band, while in p-type doping, the acceptor levels are near the valence band (Fig. 8). In the case of heavy n-type doping, donor electrons populate energy levels near the bottom of the conduction band. As electrons are fermions, they obey the Pauli Exclusion Principle, which prevents two electrons from occupying the same quantum state simultaneously. Consequently, the lower energy states at the bottom of the conduction band become fully occupied.

Because of this occupation, transitions of electrons from the valence band to these lower conduction band states are blocked. As a result, more energy is required to promote an electron from the valence band to the conduction band, increasing the optical bandgap beyond the material's fundamental bandgap. This phenomenon, known as the Burstein-Moss effect, leads to an increase in the apparent bandgap with increasing carrier concentration in n-type doped semiconductors. However, this effect (i.e., Burstein-Moss) has been reported in ZnO doped with some transition metals in some previous studies [46,47]. The science behind this phenomenon is explained by Pauli Exclusion Principle which states that electronic transition materializes at relatively higher energy levels. In other words, as the nucleation of free carriers enhances, as a consequence, blocks the chances of lower energy transitions due to Pauli Exclusion Principle forcing the high level transitions to take place [48]. This undermentioned equation exhibits the fact that apparent band gap enhances or seems higher due to addition of Burst-Moss shift. Burst- Moss shift is caused due to fermi level shifting in conduction band as a consequence of increasing free carriers or carrier concentration [46,49,50].

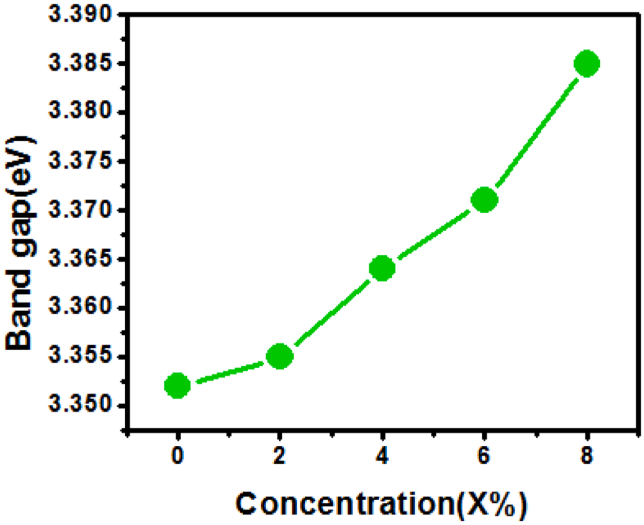

Fig. 8. Band gaps of undoped and Ni doped ZnO nanoparticles.

The relationship can be expressed as:

$$E_{g,\ apparent} = E_{g,\ actual} + \Delta E_{BM} \tag{7}$$

where $E_{g,\ apparent}$ is the observed optical bandgap, $E_{g,\ actual}$ is the fundamental bandgap, and ΔE_{BM} is the Burstein-Moss shift.

The Burstein-Moss effect causes bandgap broadening as the carrier concentration increases, making the apparent optical bandgap larger. This effect is a critical consideration in doped semiconductors, as it highlights the influence of carrier density on the electronic and optical properties, making such materials suitable for applications requiring tunable bandgaps, such as optoelectronic and photonic devices.

3.5. Dielectric Studies

3.5.1. Dielectric Constant

Dielectric properties of materials are characterized by the complex dielectric constant (ε) which is represented by:

$$\varepsilon = \varepsilon' - j\varepsilon'' \tag{8}$$

When dipoles are exposed to an external applied electric field these dipoles would be likely to align themself in the direction of applied filed in a limited time. When an external applied electric field is removed these dipoles relaxes to the original stage. The time constant for these dipoles to come their original stage is called relaxation time. In simple words polarization in materials does not respond rapidly to an applied field. The reaction which happens after a time delay compared to the applied filed can be characterized by a phase difference with the applied field.

Real and imaginary parts of dielectric constants were determined using Eq. (5) and undermentioned relationship as follows:

$$\varepsilon'' = \varepsilon' \tan\delta$$

Here tanδ is a dielectric loss. Fig. 9 demonstrates that the real part of the dielectric constant (ε') decreases with increasing frequency for all studied samples. However, the numerical value of ϵ′\epsilon'ϵ′ increases with higher nickel doping concentrations, indicating an enhancement in the semiconducting nature of Ni-doped ZnO nanoparticles. This behavior suggests that nickel doping significantly impacts the dielectric properties by introducing more charge carriers into the system.

As shown in Fig. 9, the ε' exhibits frequency-independent behavior at low frequencies, which can be attributed to Maxwell-Wagner-type relaxation [51]. According to this model, materials with inhomogeneous structures consist of grains separated by insulating grain boundaries. When an external electric field is applied, charge carriers within the grains migrate and accumulate at the grain boundaries, leading to interfacial polarization. This accumulation of charge carriers results in a high dielectric constant due to the significant polarization generated at

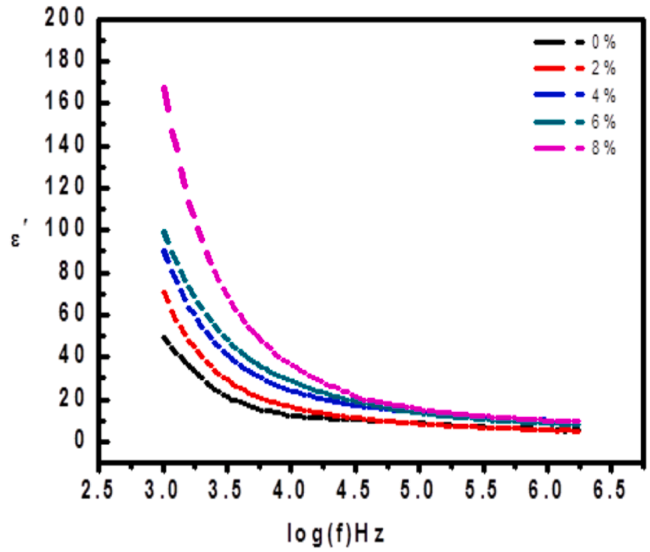

Fig. 9. Real part (ε') of a dielectric constant for all samples at various frequencies.

the interfaces.

At low frequencies, the large values of ε' can also be attributed to various factors, including oxygen vacancies, charged defects, grain boundary effects, interfacial space charge polarization, and dislocations. The structural inhomogeneity caused by grain size and porosity further contributes to this behavior. As the frequency increases, ε' decreases due to the reduced polarizability of the sample. This frequency-dependent decrease occurs because the charge carriers and dipoles cannot reorient or follow the rapidly alternating external AC electric field. Beyond a certain frequency, ε' reaches a constant value, attributed to the inability of transition metal ions, such as Ni, to respond to high-frequency electric fields. This lag in polarizability is due to the delayed response of metal ions and their associated dipoles to the applied AC field.

The polarization in ZnO doped with transition metal at relatively lower frequency $\leq 10^3$-10^4 Hz is governed by space charge polarization due material defects i.e., grain boundaries, point defects and deep trap states. This effect has been reported previously when ZnO was doped with Cr and Co [52,53]. However, in mid-range frequency range ionic conduction becomes more affective mechanism in Ni doped ZnO [54].

The decrease in ε' with frequency highlights the frequency-dependent polarization mechanisms in the material, while the increase in ε' with higher nickel doping reflects improved charge carrier density and semiconducting behavior in the Ni-doped ZnO nanoparticles. This resulted in valuable insights into the dielectric relaxation processes and the role of doping in enhancing the material's properties for potential applications in high-frequency electronic devices.

3.5.2. *Imaginary part*

The imaginary part of the dielectric constant (ϵ'') or dielectric loss represents the magnitude of the phase-shifted response in a dielectric system and is directly related to the dissipation or loss of energy. This energy dissipation occurs as charges move and polarization switches direction under the influence of an alternating electromagnetic field. The dissipated energy is converted into heat within the dielectric material, a phenomenon commonly referred to as dielectric loss. From Fig. 10, it is evident that ϵ'' decreases significantly at high frequencies. This reduction in energy dissipation at higher frequencies is attributed to the inability of ions and dipoles to follow the rapidly oscillating external electric field. As a result, the creation of dipoles diminishes, leading to lower polarization and minimal energy loss. At lower frequencies, the dissipation of energy is higher because ions and charge carriers have sufficient time to reorient and follow the applied field, contributing to interfacial and dipolar polarization. These processes lead to greater energy absorption and conversion into heat. However, as the frequency increases, the time available for dipole alignment decreases, preventing charge carriers from responding effectively to the alternating field. This results in a significant drop in ϵ'', reflecting reduced energy dissipation.

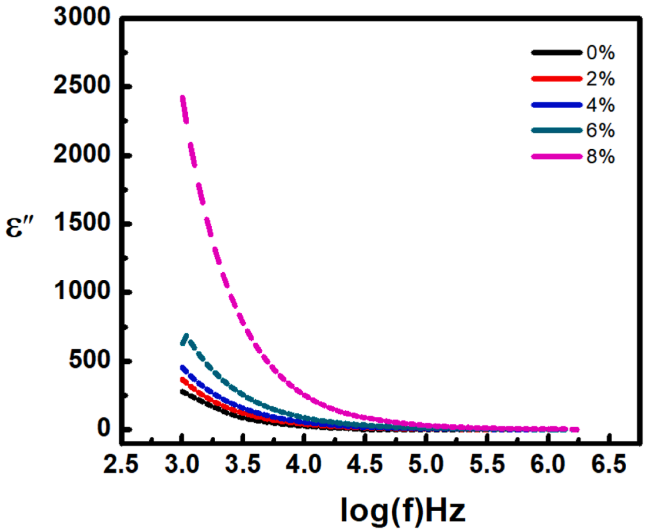

Fig. 10. Imaginary part of dielectric constant for all samples at various frequencies.

The behavior of ϵ'' provides valuable insights into the dielectric relaxation processes in the material. It highlights the frequency-dependent nature of energy dissipation, which is crucial for optimizing materials for applications such as high-frequency electronic devices, where minimizing dielectric loss is critical for energy efficiency and performance.

3.6. *Tangent loss*

The tangent loss tan δ is directly proportional to the ϵ'' of the dielectric constant, which represents energy dissipation in the dielectric system. From Fig. 11, it is evident that the tangent loss decreases as the applied frequency increases, exhibiting a dispersion behavior similar to the real part ϵ' of the dielectric constant. At lower frequencies, the tangent loss is relatively high, while at higher frequencies, it diminishes,

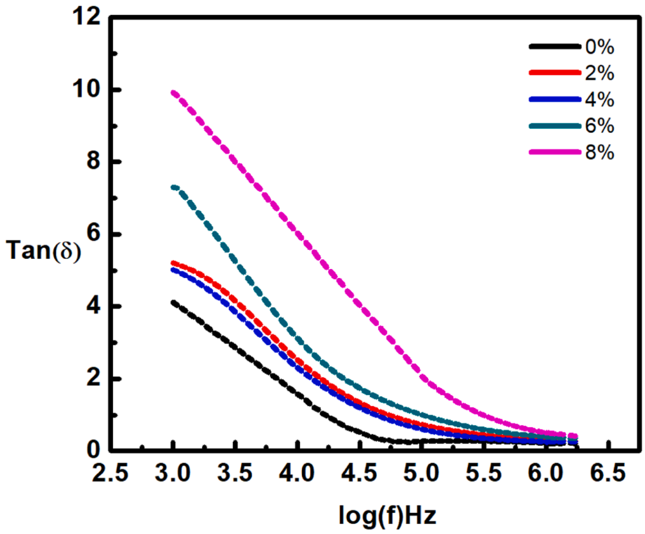

Fig. 11. Dielectric loss of pure and Ni doped ZnO nanoparticles at room temperature.

indicating reduced energy dissipation at elevated frequencies. The observed behavior at lower frequencies can be attributed to charge carriers having sufficient time to follow the alternating electric field, resulting in greater interfacial and dipolar polarization. This leads to a higher dielectric loss due to increased energy dissipation. In contrast, at higher frequencies, the rapid oscillation of the electric field prevents the charge carriers and dipoles from reorienting in time, thereby reducing energy dissipation and dielectric loss. For both undoped and Ni-doped ZnO nanoparticles, prominent dielectric loss peaks are observed at lower frequencies, known as relaxation peaks. These peaks occur when the movement of charge carriers matches the frequency of the externally applied AC electric field. This condition leads to resonance in the system, resulting in maximum energy dissipation and the observed relaxation peak [55]. Nevertheless, relaxation phenomenon has been observed to exist without any noticeable peak in $\varepsilon^{//}$ and frequency as well as in Tan (δ) vs frequency graph. This absence of peak in these graphs can be attributed towards ionic conduction in specific frequency ranges [56]. Moreover, hopping phenomenon which contributes in conductivity and may also suppress the dielectric relaxation peaks in graphs i.e., variable range hopping can limit the longer hopping of holes or charge particles which ultimately effects the relaxation. Similarly, role of interface polarization and conduction losses in mid frequency ranges can also mask the corresponding peaks in $\varepsilon^{//}$ or Tan (δ) graph plotted against frequency [57]. Moreover, in a previously conducted study on ZnO and a specific proportion on Ni Doped ZnO no prominent relaxation peak was observed in the respective frequency range i.e., logarithm of frequency ranges between 10^3 to 20^6 Hz or (take log of these values giving 3 to 6) [58,59]. Moreover, the frequency ranges in this study may not necessarily show the dominant relaxation behavior. It is quite probable that relaxation occurs below the studied frequency range.

It is also clear that the values of dielectric loss increase with higher Ni ion concentrations for all samples. This increase is due to the enhanced charge carrier density introduced by Ni doping, which promotes greater polarization and energy dissipation. The increase in dielectric loss with Ni concentration highlights the significant impact of doping on the material's electrical properties, reflecting improved charge carrier dynamics and polarization mechanisms in Ni-doped ZnO nanoparticles.

3.7. AC conductivity

The increasing behavior of AC conductivity in Ni-doped ZnO nanoparticles can be explained by the charge transport mechanism, where charge carriers are transferred between different localized states under the influence of the applied AC electric field [60]. As shown in Fig. 12, AC conductivity increases with the frequency of the external AC field for all studied samples.

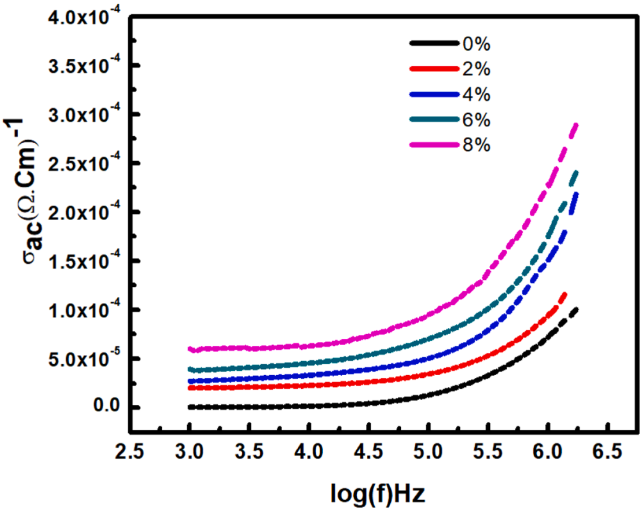

Fig. 12. Variation in ac conductivity for all samples at room temperature.

This behavior can be effectively described by the electron-hopping model. In this model, charge carriers, such as electrons, hop between lattice sites within the material. At lower frequencies, the hopping frequency of charge carriers is limited by the lower energy input from the external field, resulting in relatively low AC conductivity. However, as the frequency of the applied field increases, the energy provided by the field enables more frequent electron hopping between localized states. This increased hopping frequency leads to enhanced charge transport, resulting in higher AC conductivity.

This frequency-dependent behavior is a characteristic feature of hopping conduction, which is prevalent in doped semiconductors. The increasing AC conductivity with frequency also highlights the contribution of Ni doping, which enhances charge carrier density and facilitates better electron transport. These findings underscore the potential of Ni-doped ZnO nanoparticles for high-frequency electronic applications, where efficient charge carrier dynamics are essential for device performance.

4. Conclusions

This study successfully synthesized pure and Ni-doped ZnO nanoparticles using a co-precipitation method with varying Ni concentrations ($x = 0$, 0.02, 0.04, 0.06 and 0.08) and comprehensively evaluated their structural, optical, dielectric, and electrical properties. The XRD analysis confirmed the retention of the wurtzite hexagonal structure of ZnO, with lattice distortions observed at higher Ni doping levels. The emergence of a secondary NiO phase at $x \geq 0.06$ highlighted the solubility limit of Ni in ZnO. The crystallite size, calculated using Debye-Scherrer's equation, decreased with increasing Ni concentration due to lattice strain caused by the substitution of Zn^{2+} ions (0.74 Å) with smaller Ni^{2+} ions (0.69 Å). Optical studies revealed a systematic blue shift in the bandgap energy with increasing Ni concentration, attributed to the Burstein-Moss effect. The incorporation of Ni ions into the ZnO lattice blocked low-energy electronic transitions by filling states at the conduction band minimum, resulting in a broader apparent bandgap. FTIR spectroscopy identified functional groups and confirmed vibrational shifts due to Ni incorporation, reflecting structural changes induced by doping. Dielectric studies demonstrated that the real (ϵ') and imaginary (ϵ'') parts of the dielectric constant, as well as dielectric loss (tan δ), decreased with increasing frequency but increased with higher Ni doping levels, indicating enhanced polarization and charge carrier density. The Maxwell-Wagner relaxation model explained the interfacial polarization, while the observed relaxation peaks in dielectric loss highlighted resonance conditions where charge carriers aligned with the external AC field. AC conductivity increased with frequency, consistent with the electron-hopping model, where charge carriers transitioned between localized states, facilitated by the applied field. Ni doping enhanced charge carrier density, resulting in improved AC conductivity, particularly at higher frequencies, making the material suitable for high-frequency electronic applications. This work establishes the significant role of Ni doping in tailoring the properties of ZnO nanoparticles, demonstrating its potential for advanced applications in optoelectronics, dielectrics, and high-frequency devices.

CRediT authorship contribution statement

Muhammad Fawad: Writing – original draft, Visualization, Software, Methodology, Investigation, Formal analysis, Data curation, Conceptualization. **Nabeel Maqsood:** Writing – original draft, Visualization, Validation, Resources, Methodology, Investigation, Formal analysis. **Ahmad Nawaz:** Writing – review & editing, Visualization, Validation, Resources, Methodology, Investigation, Formal analysis. **Bilal Islam:** Writing – review & editing, Visualization, Validation, Supervision, Software, Resources, Methodology, Investigation, Formal analysis. **Malik Daniyal Zaheer:** Visualization, Validation, Resources, Investigation, Formal analysis. **Kateřina Skotnicová:** Writing – review & editing, Validation, Resources, Project administration, Investigation, Funding acquisition, Formal analysis.

Declaration of competing interest

The authors declare that they have no known competing financial interests or personal relationships that could have appeared to influence the work reported in this paper.

Funding Information

This article has been produced with the financial support of the European Union under the REFRESH – Research Excellence For REgion Sustainability and High-tech Industries project number CZ.10.03.01/00/22_003/0000048 via the Operational Programme Just Transition.

Data availability

Data will be made available on request.

References

[1] M.H. Huang, S. Mao, H. Feick, H. Yan, Y. Wu, H. Kind, E. Weber, R. Russo, P. Yang, Room-Temperature Ultraviolet Nanowire Nanolasers, Science (80-.) 292 (2001) 1897–1899, https://doi.org/10.1126/science.1060367.

[2] L.J. Brillson, W.T. Ruane, H. Gao, Y. Zhang, J. Luo, H. von Wenckstern, M. Grundmann, Spatially-resolved cathodoluminescence spectroscopy of ZnO defects, Mater. Sci. Semicond. Process. 57 (2017) 197–209, https://doi.org/10.1016/j.mssp.2016.10.032.

[3] A. Janotti, C.G. Van de Walle, Fundamentals of zinc oxide as a semiconductor, Reports Prog. Phys. 72 (2009) 126501, https://doi.org/10.1088/0034-4885/72/12/126501.

[4] R. Nandee, M.A. Chowdhury, N. Hossain, M.M. Rana, M.H. Mobarak, M.A. Islam, H. Aoyon, Experimental characterization of defect-induced Raman spectroscopy in graphene with BN, ZnO, Al2O3, and TiO2 dopants, Results Eng. 21 (2024) 101738, https://doi.org/10.1016/j.rineng.2023.101738.

[5] Z.L. Wang, Zinc oxide nanostructures: growth, properties and applications, J. Phys. Condens. Matter. 16 (2004) R829–R858, https://doi.org/10.1088/0953-8984/16/25/R01.

[6] N. Hossain, M.H. Mobarak, M.A. Mimona, M.A. Islam, A. Hossain, F.T. Zohura, M. A. Chowdhury, Advances and significances of nanoparticles in semiconductor applications – A review, Results Eng 19 (2023) 101347, https://doi.org/10.1016/j.rineng.2023.101347.

[7] Y. Liu, Z.H. Kang, Z.H. Chen, I. Shafiq, J.A. Zapien, I. Bello, W.J. Zhang, S.T. Lee, Synthesis, Characterization, and Photocatalytic Application of Different ZnO Nanostructures in Array Configurations, Cryst. Growth Des. 9 (2009) 3222–3227, https://doi.org/10.1021/cg801294x.

[8] C.S. Damian, D. Yuvarajan, T. Raja, G. Choubey, D.B. Munuswamy, Biodiesel production from shrimp shell lipids: Evaluating ZnO nanoparticles as a catalyst, Results Eng. 24 (2024) 103453, https://doi.org/10.1016/j.rineng.2024.103453.

[9] Z.W. Pan, Z.R. Dai, Z.L. Wang, Nanobelts of Semiconducting Oxides, Science (80-.) 291 (2001) 1947–1949, https://doi.org/10.1126/science.1058120.

[10] N. Maqsood, A. Khan, M.K. Alamgir, S.A. Shah, M. Fahad, PTFE Thin Film Coating on 316L Stainless Steel for Corrosion Protection in Acidic Environment, J. Eng. Appl. Sci. 36 (2017) 183–190.

[11] M. Samadi, M. Zirak, A. Naseri, E. Khorashadizade, A.Z. Moshfegh, Recent progress on doped ZnO nanostructures for visible-light photocatalysis, Thin Solid Films 605 (2016) 2–19, https://doi.org/10.1016/j.tsf.2015.12.064.

[12] V. Gandhi, R. Ganesan, H.H. Abdulrahman Syedahamed, M. Thaiyan, Effect of Cobalt Doping on Structural, Optical, and Magnetic Properties of ZnO Nanoparticles Synthesized by Coprecipitation Method, J. Phys. Chem. C. 118 (2014) 9715–9725, https://doi.org/10.1021/jp411848t.

[13] Y. Xia, J. Wang, R. Chen, D. Zhou, L. Xiang, A Review on the Fabrication of Hierarchical ZnO Nanostructures for Photocatalysis Application, Crystals 6 (2016) 148, https://doi.org/10.3390/cryst6110148.

[14] J. Vera, W. Herrera, E. Hermosilla, H. Schalchli, R. Díaz, P. Fincheira, A.B. Seabra, A. Quiroz, G. Tortella, O. Rubilar, Photodegradation of lignin biowaste catalyzed by biosynthesized zinc oxide nanoparticles using the leaf extract of Aristotelia chilensis, Results Eng 25 (2025) 103866, https://doi.org/10.1016/j.rineng.2024.103866.

[15] B. Kramer (Ed.), Advances in Solid State Physics, Springer Berlin Heidelberg, Berlin, Heidelberg, 2003, https://doi.org/10.1007/b12017.

[16] S. Raha, M. Ahmaruzzaman, ZnO nanostructured materials and their potential applications: progress, challenges and perspectives, Nanoscale Adv 4 (2022) 1868–1925, https://doi.org/10.1039/D1NA00880C.

[17] Q. Hao, S. Liu, X. Yin, Z. Du, M. Zhang, L. Li, Y. Wang, T. Wang, Q. Li, Flexible morphology-controlled synthesis of mesoporous hierarchical α-Fe2O3 architectures and their gas-sensing properties, CrystEngComm 13 (2011) 806–812, https://doi.org/10.1039/C0CE00194E.

[18] V. Gandhi, R. Ganesan, H.H. Abdulrahman Syedahamed, M. Thaiyan, Effect of Cobalt Doping on Structural, Optical, and Magnetic Properties of ZnO Nanoparticles Synthesized by Coprecipitation Method, J. Phys. Chem. C. 118 (2014) 9715–9725, https://doi.org/10.1021/jp411848t.

[19] D. Guruvammal, S. Selvaraj, S.Meenakshi Sundar, Effect of Ni-doping on the structural, optical and magnetic properties of ZnO nanoparticles by solvothermal method, J. Alloys Compd. 682 (2016) 850–855, https://doi.org/10.1016/j.jallcom.2016.05.038.

[20] P.S. Menon, M.P. Anjana, A.K. Jose, J. Kunjumon, A. PA, S. Chandran, M. George, G. Vinitha, D. Sajan, The role of defects on linear and nonlinear optical properties of pristine and nickel doped zinc oxide nanoparticles, Surfaces and Interfaces 34 (2022) 102393, https://doi.org/10.1016/j.surfin.2022.102393.

[21] J. El Ghoul, N. Abdel All, G. Khouqeer, M.S. Alshammari, Structural, Optical and Magnetic Properties of (Al, Ni) Co-Doped ZnO Nanoparticles, J. Nanoelectron. Optoelectron. 16 (2021) 1372–1379, https://doi.org/10.1166/jno.2021.3091.

[22] S.B. Rana, R.P.P. Singh, Investigation of structural, optical, magnetic properties and antibacterial activity of Ni-doped zinc oxide nanoparticles, J. Mater. Sci. Mater. Electron. 27 (2016) 9346–9355, https://doi.org/10.1007/s10854-016-4975-6.

[23] M.A. Ansari, N. Jahan, A Novel Co-Precipitation Route for the Synthesis of Pure and Ni-Doped CuO Nanoparticles: Effect of Doping on Structural, Optical, and Electrical Properties, Int. J. Nanosci. Nanotechnol. 19 (2023) 65–76, https://doi.org/10.22034/ijnn.2023.555186.2219.

[24] F.M. Hussein, Doped ZnO Nanostructured and their application as photocatalytic: as Review, J. Adv. Sci. Eng. Technol. 4 (2021) 1–15, https://doi.org/10.32441/jaset.04.01.01.

[25] J. Mathew, G. Varghese, J. Mathew, Structural and Optical Properties of Ni:ZnO Thin Films-Effect of Annealing and Doping Concentration, SOP Trans. Appl. Phys. (2014) 27–36, https://doi.org/10.15764/APHY.2014.04003.

[26] I. Riwayati, S. Winardi, S. Madhania, M. Shimada, Kusdianto, Green synthesis of ZnO nanoparticles using Cosmos caudatus: Effects of calcination temperature and precursor type on photocatalytic and antimicrobial activities, Results Eng 24 (2024) 103594, https://doi.org/10.1016/j.rineng.2024.103594.

[27] V. Srikant, D.R. Clarke, On the optical band gap of zinc oxide, J. Appl. Phys. 83 (1998) 5447–5451, https://doi.org/10.1063/1.367375.

[28] T. Bora, K.K. Lakshman, S. Sarkar, A. Makhal, S. Sardar, S.K. Pal, J. Dutta, Modulation of defect-mediated energy transfer from ZnO nanoparticles for the photocatalytic degradation of bilirubin, Beilstein J. Nanotechnol. 4 (2013) 714–725, https://doi.org/10.3762/bjnano.4.81.

[29] R.K. Gupta, A. Motallebzadeh, S. Kakooei, T.A. Nguyen, A. Behera, Advanced Ceramic Coatings: Fundamentals, Manufacturing, and Classification, Elsevier, 2023.

[30] W. Habib, A. Saji, F. Paul, P.R. Markapudi, C. Wilson, L. Manjakkal, Flexible electrochemical capacitors based on ZnO-carbon black composite, Results Eng 25 (2025) 104510, https://doi.org/10.1016/j.rineng.2025.104510.

[31] A.E. Adeoye, C.V O, V. Owoeye, E.D. Ogunmola, Structural, Optical and Rectifying Properties of Spray Deposited Ni doped and undoped ZnO Thin Films, IOSR J. Humanit. Soc. Sci. 26 (2021) 46–52, https://doi.org/10.9790/0837-2606014652.

[32] M. Gad, A. Abd-Elghany, R. IBRAHIM, T. ALI, Structural modification and characterization of Sn-Zn eutectic alloy doped with copper oxide nanoparticles, Alfarama J. Basic Appl. Sci. (2023), https://doi.org/10.21608/ajbas.2023.235429.1181, 0–0.

[33] Y. Slimani, M.J.S. Mohamed, R. Sivakumar, M.A. Gondal, R. Vignesh, A. Thakur, A. Baykal, M. Nawaz, M.A. Almessiere, Enhancing the Light-Driven Photocatalytic Degradation Activity of ZnO Nanoparticles With the Synergistic Incorporation of Er and Tb Elements, Appl. Organomet. Chem. (2024), https://doi.org/10.1002/aoc.7863.

[34] U. Godavarti, V.D. Mote, M. Dasari, Precipitated nickel doped ZnO nanoparticles with enhanced low temperature ethanol sensing properties, Mod. Electron. Mater. 3 (2017) 179–185, https://doi.org/10.1016/j.moem.2017.10.006.

[35] Z. Wei, H. Qiao, H. Yang, C. Zhang, X. Yan, Characterization of NiO nanoparticles by anodic arc plasma method, J. Alloys Compd. 479 (2009) 855–858, https://doi.org/10.1016/j.jallcom.2009.01.064.

[36] B.N. Dole, V.D. Mote, V.R. Huse, Y. Purushotham, M.K. Lande, K.M. Jadhav, S. S. Shah, Structural studies of Mn doped ZnO nanoparticles, Curr. Appl. Phys. 11 (2011) 762–766, https://doi.org/10.1016/j.cap.2010.11.050.

[37] A.J. Reddy, M.K. Kokila, H. Nagabhushana, R.P.S. Chakradhar, C. Shivakumara, J. L. Rao, B.M. Nagabhushana, Structural, optical and EPR studies on ZnO:Cu nanopowders prepared via low temperature solution combustion synthesis, J. Alloys Compd. 509 (2011) 5349–5355, https://doi.org/10.1016/j.jallcom.2011.02.043.

[38] C.K. Ghosh, S. Malkhandi, M.K. Mitra, K.K. Chattopadhyay, Effect of Ni doping on the dielectric constant of ZnO and its frequency dependent exchange interaction, J. Phys. D. Appl. Phys. 41 (2008) 245113, https://doi.org/10.1088/0022-3727/41/24/245113.

[39] G. Srinet, R. Kumar, V. Sajal, Structural, optical, vibrational, and magnetic properties of sol-gel derived Ni doped ZnO nanoparticles, J. Appl. Phys. 114 (2013), https://doi.org/10.1063/1.4813868.

[40] G. Srinet, R. Kumar, V. Sajal, Effects of Ni doping on structural, optical and dielectric properties of ZnO, Ceram. Int. 39 (2013) 7557–7561, https://doi.org/10.1016/j.ceramint.2013.03.008.

[41] J. Jadhav, S. Biswas, Shape-controlled magnetic nanoplatelets of Ni-doped ZnO synthesized via a chemical precursor, J. Alloys Compd. 664 (2016) 71–82, https://doi.org/10.1016/j.jallcom.2015.12.191.

[42] E. Liu, P. Xiao, J.S. Chen, B.C. Lim, L. Li, Ni doped ZnO thin films for diluted magnetic semiconductor materials, Curr. Appl. Phys. 8 (2008) 408–411, https://doi.org/10.1016/j.cap.2007.10.025.

[43] C.-Y. Chen, M. Wang, J.-Y. Li, N. Pootrakulchote, L. Alibabaei, C. Ngoc-le, J.-D. Decoppet, J.-H. Tsai, C. Grätzel, C.-G. Wu, S.M. Zakeeruddin, M. Grätzel, Highly Efficient Light-Harvesting Ruthenium Sensitizer for Thin-Film Dye-Sensitized Solar Cells, ACS Nano 3 (2009) 3103–3109, https://doi.org/10.1021/nn900756s.

[44] W. Yu, L.H. Yang, X.Y. Teng, J.C. Zhang, Z.C. Zhang, L. Zhang, G.S. Fu, Influence of structure characteristics on room temperature ferromagnetism of Ni-doped ZnO thin films, J. Appl. Phys. 103 (2008), https://doi.org/10.1063/1.2903524.

[45] B. Philips-Invernizzi, Bibliographical review for reflectance of diffusing media, Opt. Eng. 40 (2001) 1082, https://doi.org/10.1117/1.1370387.

[46] A. Hassan, Y. Jin, M. Irfan, Y. Jiang, Acceptor-modulated optical enhancements and band-gap narrowing in ZnO thin films, AIP Adv 8 (2018), https://doi.org/10.1063/1.5020830.

[47] C. Mahata, I.-K. Oh, C.M. Yoon, C.W. Lee, J. Seo, H. Algadi, M.-H. Sheen, Y.-W. Kim, H. Kim, T. Lee, The impact of atomic layer deposited SiO 2 passivation for high-k Ta 1−x Zr x O on the InP substrate, J. Mater. Chem. C. 3 (2015) 10293–10301, https://doi.org/10.1039/C5TC01890K.

[48] N.R. Yogamalar, A.Chandra Bose, Burstein–Moss shift and room temperature near-band-edge luminescence in lithium-doped zinc oxide, Appl. Phys. A. 103 (2011) 33–42, https://doi.org/10.1007/s00339-011-6304-5.

[49] Q. Zhu, C. Xie, H. Li, C. Yang, S. Zhang, D. Zeng, Selectively enhanced UV and NIR photoluminescence from a degenerate ZnO nanorod array film, J. Mater. Chem. C. 2 (2014) 4566, https://doi.org/10.1039/c4tc00011k.

[50] C.E. Kim, P. Moon, S. Kim, J.-M. Myoung, H.W. Jang, J. Bang, I. Yun, Effect of carrier concentration on optical bandgap shift in ZnO:Ga thin films, Thin Solid Films 518 (2010) 6304–6307, https://doi.org/10.1016/j.tsf.2010.03.042.

[51] D. Maseda, J.P. Zackular, B. Trindade, L. Kirk, J.L. Roxas, L.M. Rogers, M. K. Washington, L. Du, T. Koyama, V.K. Viswanathan, G. Vedantam, P.D. Schloss, L. J. Crofford, E.P. Skaar, D.M. Aronoff, Nonsteroidal Anti-inflammatory Drugs Alter the Microbiota and Exacerbate Clostridium difficile Colitis while Dysregulating the Inflammatory Response, MBio 10 (2019), https://doi.org/10.1128/mBio.02282-18.

[52] R.N. Aljawfi, F. Rahman, K.M. Batoo, Effect of grain size and grain boundary defects on electrical and magnetic properties of Cr doped ZnO nanoparticles, J. Mol. Struct. 1065–1066 (2014) 199–204, https://doi.org/10.1016/j.molstruc.2014.02.056.

[53] A.A. Sasikala Devi, I.S. Roqan, The origin of room temperature ferromagnetism mediated by Co–V Zn complexes in the ZnO grain boundary, RSC Adv 6 (2016) 50818–50824, https://doi.org/10.1039/C6RA11607H.

[54] O. Hafef, Z.J. Othman, M. Megdich, A. Matoussi, Conduction mechanism and dielectric properties of ZnO/MgO solid composites, Appl. Phys. A. 123 (2017) 95, https://doi.org/10.1007/s00339-016-0721-4.

[55] A. Abdeen, O. Hemeda, E. Assem, M. El-Sehly, Structural, electrical and transport phenomena of Co ferrite substituted by Cd, J. Magn. Magn. Mater. 238 (2002) 75–83, https://doi.org/10.1016/S0304-8853(01)00465-6.

[56] A.A. SAIF, Z.A. ZAHID JAMAL, Z. SAULI, P. POOPALAN, Frequency Dependent Electrical Properties of Ferroelectric Ba0.8Sr0.2TiO3 Thin Film, Mater. Sci. 17 (1970) 186–190, https://doi.org/10.5755/j01.ms.17.2.490.

[57] L. Cao, R. Xi, C. Zhou, G. He, F. Yang, L. Xu, H. Li, Polymer Capacitor Films with Nanoscale Coatings for Dielectric Energy Storage: A Review, Coatings 14 (2024) 1193, https://doi.org/10.3390/coatings14091193.

[58] P. Norouzzadeh, K. Mabhouti, M.M. Golzan, R. Naderali, Comparative study on dielectric and structural properties of undoped, Mn-doped, and Ni-doped ZnO nanoparticles by impedance spectroscopy analysis, J. Mater. Sci. Mater. Electron. 31 (2020) 7335–7347, https://doi.org/10.1007/s10854-019-02517-0.

[59] R. Rathnasekara, G. Mayberry, P. Hari, Thermoelectric, Electrochemical, & Dielectric Properties of Four ZnO Nanostructures, Materials (Basel) 15 (2022) 8816, https://doi.org/10.3390/ma15248816.

[60] M.A. Ahmed, E. Ateia, S.I. El-Dek, Rare earth doping effect on the structural and electrical properties of Mg–Ti ferrite, Mater. Lett. 57 (2003) 4256–4266, https://doi.org/10.1016/S0167-577X(03)00300-8.